## Twisted Bilayer Graphene Reveals its Flat Bands under Spin Pumping

Stacking two graphene layers with a relative twist angle $\theta$ results in a moiré superstructure which is found to host, in the vicinity of the so-called magic angle $\theta_M$ 1.1˚, unconventional superconductivity and strongly correlated insulating states [1,2]. Such strong electronic correlations originate from the moiré flat bands emerging at the magic angle around the charge neutrality point. The tantalizing signature of the flat bands have been experimentally demonstrated by probing the corresponding peaks of the density of states using transport, electronic compressibility measurements, scanning tunneling microscopy (STM) and spectroscopy (STS). The direct evidence of these flat bands has been reported by angle resolved photoemission spectroscopy (ARPES). However, spectroscopic measurements on magic-angle twisted bilayer graphene (TBG) raise many technical challenges related to the need of an accurate control of the twist angle, and the necessity to have non-encapsulated samples which can degrade in air.

Recently, we proposed a noninvasive method to probe the flat bands of TBG and accurately determine the magic angle [3]. This method is based on spin pumping induced by ferromagnetic resonance, where the increase in the FMR linewidth provides insight into the spin excitations of the nonmagnetic material adjacent to the ferromagnet. The linewidth increase is given by the Gilbert damping (GD) coefficient.

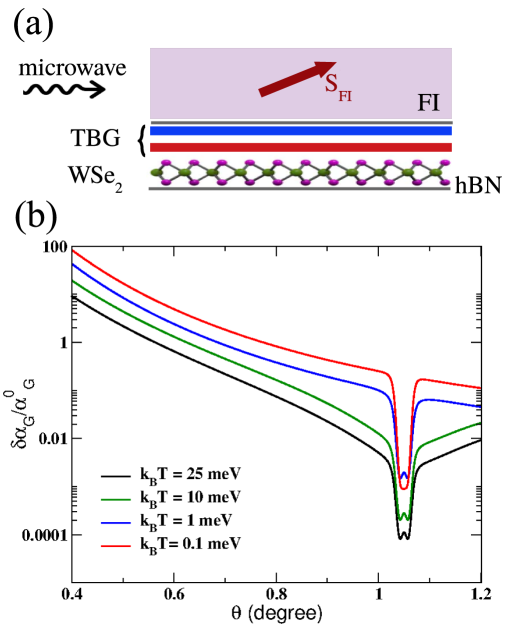


Fig. 1. (a) Schematic representation of the junction between a ferromagnetic insulator (FI) and a heterostructure of a twisted bilayer graphene (TBG) adjacent to a monolayer of $WSe_2$. The red arrow indicates the spin orientation of the FI characterized by an average spin. The bottom line represents the boron-nitride (hBN) layers encapsulating the TBG/$WSe_2$ heterostructure. (b) Increase of the Gilbert damping coefficient, $\delta\alpha_G$, as a function of the twist angle at different temperature ranges.

We theoretically study a planar junction of a ferromagnetic insulator (FI) and a TBG adjacent to a monolayer of transition metal dichalcogenides (TMD), as $WSe_2$ (TBG/$WSe_2$). We show a schematic figure of a FI/TBG planar junction adjacent to $WSe_2$ under a microwave of a frequency $\Omega$ in Fig. 1 (a). We consider the case where a microwave of a frequency $\Omega$ is applied to this junction and focus on the twist angle dependence of the FMR linewidth. We calculated the correction to the Gilbert damping (GD) coefficient, induced by the adjacent heterostructure TBG/$WSe_2$. We take into account the relatively strong spin-orbit interaction (SOI) induced by the $WSe_2$ in TBG.

We formulated the FMR linewidth based on the perturbation method with respect to an interfacial exchange coupling in this setup and discussed its twist angle dependence. We described the heterostructure TBG/$WSe_2$ by the continuum model including the SOI based on Ref. [4] and evaluated the increase of the effective Gilbert damping coefficient of the FMR linewidth.

In Fig. 1(b) we depicted the behavior of $\delta\alpha_G$ as a function of the twist angle $\theta$ for several temperatures for a clean interface. This figure shows that regardless of the temperature range, $\delta\alpha_G$ increases by decreasing $\theta$ but drops sharply at the magic angle, where it exhibits a relatively small peak which is smeared out at low temperature. We also discussed the case of a dirty interface and showed that the Gilbert damping correction drops at the magic angle as found in the case of a clean interface.

Our result provides an accurate determination method of the magic angle and an estimation of the SOC induced in TBG by its proximity to the TMD layer. Our proposed setup can be readily implemented regarding the state-of-the art of the experimental realizations of spin pumping in 2D materials and TBG-based heterostructure. Our work opens the gate to a twist tunable spintronics in twisted layered heterostructures.

This project has been performed as a joint study with Sonia Haddad, who was a visiting professor of ISSP in the academic year 2022.

**References**

[1] Y. Cao *et al.*, Nature, **556**, 80 (2018).
[2] M. Yankowitz *et al.*, Science **363**, 1059 (2019).
[3] S. Haddad, T. Kato, J. Zhu, and L. Mandhour, Phys. Rev. B **108**, L121101 (2023).
[4] H. S. Arora *et al.*, Nature **583**, 379 (2020).

**Authors**
S. Haddad[a,b], T. Kato, J. Zhu[b], and L. Mandhour[a]
[a]Université Tunis El Manar
[b]Max Planck Institute for the Physics of Complex Systems

PI of Joint-use project: S. Haddad
Host lab: Kato and Osada Groups

# Element-Specific Cluster Growth on the Two-Dimensional Metal–Organic Network

Solid surfaces provide a platform to fabricate various low-dimensional structures, and the formation of surface-supported two-dimensional metal–organic networks (2D-MONs) based on supramolecular chemistry is also achieved on the substrate. Porous two-dimensional metal–organic network (2D-MON) on a substrate could capture deposited metal atoms and metal clusters growing in the pores of the 2D-MON. Growth of a metal cluster in a pore of the 2D-MON requires that the pore is a local minimum of the potential energy surface, that is, a potential well for the metal adatoms. By arranging nanometer-scale potential wells on the substrate, deposited metal atoms form metal nanoclusters spontaneously.

We investigated the growth of Ag, In, and Pd nanoclusters in the 2D-MON by scanning tunneling microscopy (STM) measurements and density functional theory (DFT) calculations, and found that the growth mechanisms of Ag, In, and Pd clusters in the 2D-MON synthesized from 1,3,5-tris(4-bromophenyl) benzene molecules on Ag(111) are different from each other. From the STM measurement, Ag and Pd clusters grow from the 2D-MON, especially two-coordinated Ag atoms in the 2D-MON. Indium clusters grow in the center of pores. Based on our DFT calculations, the total energy of an adatom in a pore depends on the position of the adatom, and the interaction of Ag and Pd adatoms with the 2D-MON is attractive. On the other hand, the interaction between an In adatom and the 2D-MON is repulsive. Since the net-charges of Ag, In, Pd adatoms on Cu(111), and two-coordinated Ag in the 2D-MON are −0.01e, 0.38e, and −0.14e, and 0.23e, respectively, the electrostatic interaction between In and Pd adatoms and the 2D-MON may play a significant role. For Ag, the DFT calculation without van-der Waals correction results in repulsive interaction with the 2D-MON. We think that van-der Waals interaction plays an important role in the Ag nanocluster formation in the 2D-MON. The growth process of metal clusters is determined by the element-specific behavior of metal adatoms in the pores, taking into account the various interactions with the 2D-MON.

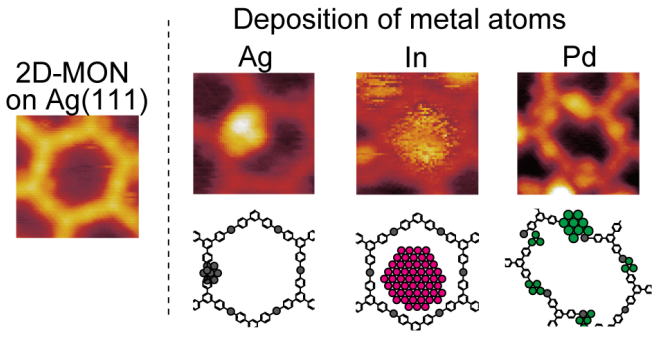


Fig. 1. (Left) An STM image of the 2D-MON on Ag(111). (Right) STM images of Ag (gray), In (red), and Pd (green) clusters on the 2D-MON/Ag(111) surface and their schematic drawings. The size of all STM images is 4 nm × 4 nm.

**Reference**
[1] N. Tsukahara, R. Arafune, and J. Yoshinobu, Jpn. J. Appl. Phys. **63**, 065504 (2024).

**Authors**
N. Tsukahara[a], R. Arafune[b], and J. Yoshinobu
[a]National Institute of Technology, Gunma College.
[b]National Institute for Materials Science

PI of Joint-use project: N. Tsukahara
Host lab: Yoshinobu Group

# $Y_2O_3$ Phosphor Thin Films

When thin film materials are grown by physical vapor deposition methods, such as sputtering or pulsed laser deposition (PLD), the kinetic energy of the adatoms arriving on the film surface has a significant effect on the crystallinity and defect density of thin films. In the PLD process, the incident adatom kinetic energy can reach 100 eV or more. The kinetic energy is increased at higher ablation laser energy density (laser pulse energy) due to a larger energy transfer from the laser beam to the ablated plasma. The kinetic energy is also dependent on the temporal ablation laser pulse shape. For typical excimer gas lasers, the pulse length is 20 ns, while solid-state garnet (YAG) lasers generate around 4 ns pulses, which means that the pulse rise time is faster for YAG lasers, leading to higher plasma kinetic energies. One of the advantages of PLD is the ability to use a very broad background gas pressure range, from a typical base pressure of $10^{-8}$ Torr to about 1 Torr. Increasing the process pressure of a background gas, such as oxygen, above 1 mTorr will increase the number of gas-phase collisions between ions in the ablation plume and the ambient gas, reducing the kinetic energy of the plume. However, high-pressure ablation also strongly reduces the growth rate, as many atoms colliding with the ambient gas are deflected from the plume and do not reach the film surface. We have developed an energy-moderated PLD technique using He as a buffer gas in the PLD chamber to reduce the kinetic energy of the plume. Due to the small mass of He, the gas-phase collisions reduce the plasma energy but do not deflect the atoms away from the plume, allowing films to be grown at the desired growth rate, but at a lower incident kinetic energy of deposited atoms, reducing the density of point defects in the film. The point defect density is a particularly serious problem for optical materials, such as phosphors,

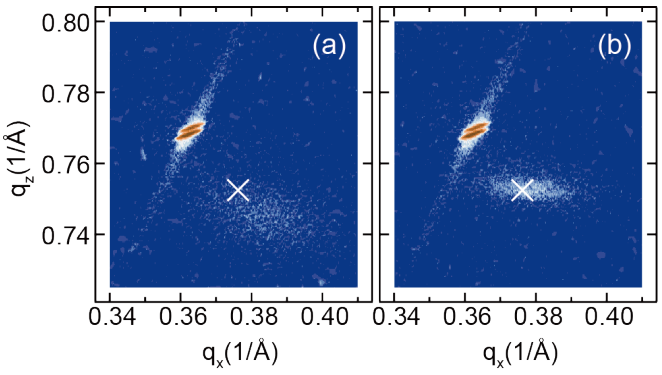


Fig. 1. X-ray reciprocal space maps of $Y_2O_3$ films grown on $SrTiO_3$ at an oxygen pressure of $10^{-4}$ Torr (a) and in a mixture of $10^{-4}$ Torr $O_2$ and 100 mTorr He. The addition of the He buffer increased the film peak intensity, reduced the peak width, and shifted the film peak close to the expected bulk lattice parameter (marked with a white cross).

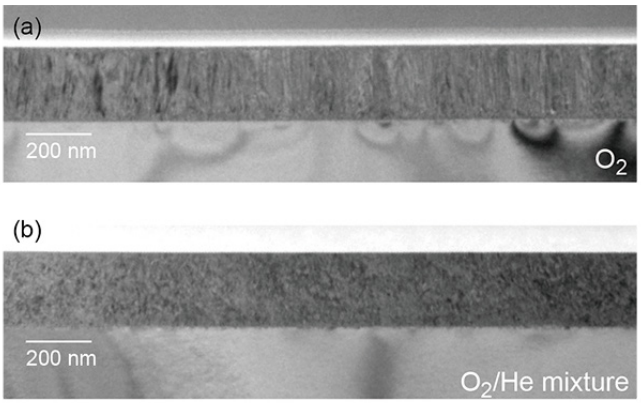


Fig. 2. Cross-sectional transmission electron microscope images of a film grown in oxygen (a), showing distinct columnar grains, and in an oxygen/helium mixture (b), showing that the grain boundaries were eliminated in the presence of the energy-moderating He buffer gas in the PLD chamber.

where defects reduce the intensity and the lifetime of the luminescence signal. We have explored the effect of plume energy moderation on the properties of PLD-grown $Y_2O_3$ phosphors. The effect of the energy moderation can be seen in the x-ray reciprocal space maps of two films (Fig. 1), both grown at an oxygen partial pressure of $10^{-4}$ Torr. A film grown in a conventional process (Fig. 1a) shows diffuse film scattering that is systematically shifted from the expected lattice parameter (marked with a white cross). When the PLD chamber is additionally filled to 100 mTorr with He, the film peak becomes much narrower and shifts to the expected bulk lattice parameter position, indicating that the crystalline defect density was dramatically reduced by the plume energy reduction. The microstructure change is clearly visible in cross-sectional transmission electron microscope images of films grown in a low-pressure oxygen environment and in the presence of He gas at a pressure of 100 mTorr (Fig. 2). When a $Y_2O_3$ film was grown under conventional conditions, without the He moderator, the film formed columnar grains that extend through the thickness of the film. Such grain boundaries can effectively quench the light output of a phosphor material. This columnar structure was completely eliminated when a film was grown in a $He/O_2$ gas mixture at a total pressure of 100 mTorr. Time-of-flight measurements indicated that the kinetic energy of the plume was reduced by a factor of about 7 at 100 mTorr of He. The reduction of the defect density of the films significantly increased the photoluminescence intensity of the Eu-doped yttria phosphor films.

**References**
[1] S. Suzuki, T. Dazai, T. Tokunaga, T Yamamoto, R. Katoh, M. Lippmaa, and R. Takahashi, J. Appl. Phys. **135**, 195302 (2024).

**Authors**
S. Suzuki[a], T. Dazai[a], T. Tokunaga[b], T Yamamoto[b], R. Katoh[a], M. Lippmaa, and R. Takahashi[a]
[a] Nihon University
[b]Nagoya University

PI of Joint-use project: R. Takahashi
Host lab: Lippmaa Group

# Spin fluctuations from Bogoliubov Fermi Surfaces in the Superconducting State of S-substituted FeSe

The study of the iron-based superconductor, $FeSe_{1-x}S_x$, has resulted in various topics. Recently, topologically protected nodal Fermi surfaces, referred to as Bogoliubov Fermi surfaces (BFSs), have garnered much attention [1,2]. A theoretical model for $FeSe_{1-x}S_x$ demonstrated that BFSs can manifest under the conditions of spin-orbit coupling, multi-band systems, and superconductivity with time-reversal symmetry breaking [1]. Here we report the observation of spin fluctuations originating from BFSs via $^{77}$Se-nuclear magnetic resonance (NMR) measurements to 100 mK [3]. We found an anomalous enhancement of low-energy spin fluctuations deep in the superconducting (SC) state for $x = 0.18$, which gives evidence for strong Bogoliubov quasiparticles interactions in addition to the presence of BFSs.

We performed $^{77}$Se-NMR measurements using a single crystal for each S-substitution level. Typical size is approximately $1.0 \times 1.0 \times 0.5$ mm. We applied a magnetic field of 6.0 T parallel to the FeSe planes. Figure 1 shows $1/T_1T$ below $T_c$ for several S-substitution levels crossing the nematic quantum critical point, $x_c \sim 0.17$. As seen from $^{77}$Se-NMR spectra in Fig. 2, the double-peaks structure observed in the nematic phase disappears above $x_c$. $1/T_1T$ provides a measure of low-energy spin fluctuations and is expressed as $1/T_1T \propto \sum_q Im\chi(\mathbf{q})$, where $\chi(\mathbf{q})$ is the wave-number ($\mathbf{q}$)-dependent susceptibility. The decrease in

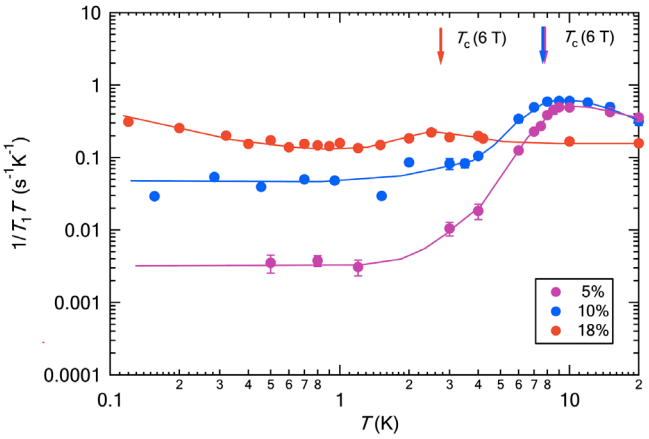


Fig. 1. $^{77}$Se-nuclear relaxation rate divided by temperature, $1/T_1T$ for $FeSe_{1-x}S_x$ ($x = 0.05$, 0.10, and 0.18) [3]. Arrows indicate superconducting transition temperature ($T_c$) measured at 6.0 T.

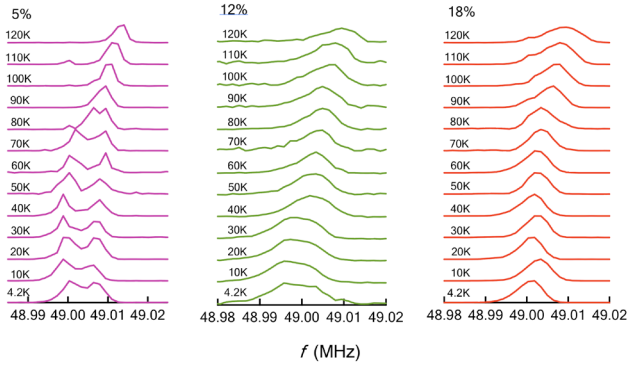


Fig. 2. $^{77}$Se-NMR spectra for $x = 0.05$, 0.12, and 0.18 [3]. Two peaks appearing for $x = 0.05$ and 0.12 merge into a single peak with increasing S-substitution level over $x_c$ ($\geq 0.17$).

$1/T_1T$ just below $T_c$ is due to the opening of the SC gap. In conventional clean superconductors, $1/T_1T$ should decrease to zero with decreasing temperature. However, $1/T_1T$ for $x = 0.05$ and 0.10 became constant at low temperatures. With further substitution over $x_c$, $1/T_1T$ exhibited an upturn with decreasing temperature and the values became significantly larger than those for $x = 0.05$ and 0.10. Upturns of $1/T_1T$ observed below and above $T_c$ are exceedingly rare in SC systems. The behavior of $1/T_1T = constant$ suggests a residual DOS. In most cases, the following effects may be expected: (1) the impurity effect, (2) the Volovik effect, and (3) the coexistence of SC and normal states. However, the first two cases are ruled out because the values of $1/T_1T$ change almost one order of magnitude between $x = 0.05$ and 0.10, and the last case is also ruled out considering the high sample quality. Furthermore, the upturn of $1/T_1T$ is difficult to be explained by these possibilities. Instead of the coexistence in real space, the coexistence in momentum space such as the formation of BFSs would be promising as shown in Fig. 3. The appearance of BFSs with two-hold rotational symmetry has been observed by laser ARPES measurements [4] and time-reversal-symmetry breaking required for the appearance of BFSs has been suggested from recent μSR measurements [5].

Recently, Y. Cao *et al.* theoretically calculated $\chi(\mathbf{q})$ and $1/T_1T$ for the ultranodal states in a minimal two-band model, where the interband non-unitary spin-triplet pairing is responsible for BFSs [6]. In this model, they assumed double hole pockets at the Γ point and BFSs with two-fold rotational symmetry like the schematic diagram shown in Fig. 3. By adding a Hubbard interaction in the particle-hole channel, they found that an enhancement of $\chi(\mathbf{q})$ at low temperatures at $\mathbf{q}$~(0.4π, 0) connecting coherent segments/spots on the BFSs when the interaction is strong. This leads to an upturn of $1/T_1T$ at low temperatures like experimental results of $x = 0.18$. In this model, the upturn can be derived based on the minimal two-band model at the Γ point, while the $T$ dependence of $1/T_1T$ below $T_c$ is similar to that above $T_c$, implying that the nesting between the hole and electron pockets would be responsible for the upturn of $1/T_1T$ below $T_c$ [3]. It remains a future problem whether the nesting contributes to the upturn of $1/T_1T$.

The presence of BFSs below $x_c$ makes it easy to comprehend $1/T_1T$ =*constant*. The values of $1/T_1T$ for $x = 0.05$ or 0.10 are one or two orders of magnitude smaller than those for $x = 0.18$, implying that the BFSs should be much smaller and the interactions should be suppressed. In such case, the upturn of $1/T_1T$ is hardly expected and $1/T_1T$ =*constant* is attributed to the scattering between a nucleus and almost free Bogoliubov quasiparticles like the Korringa relation in conventional metals. It should be noted that such relaxation process is realized not in the normal state but in the SC state. In the Korringa relation, $1/T_1T$ is proportional to square of the DOS. The difference of $1/T_1T$ in one order of magnitude between $x = 0.05$ and 0.10 implies that the quasiparticle DOS differs almost three times between them. Our results suggest that BFSs exist even below $x_c \sim 0.17$ and expand with increasing S-substitution level.

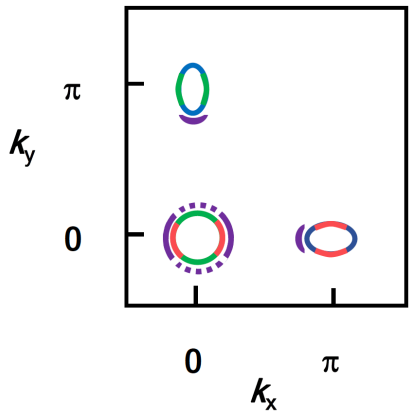


Fig. 3. Schematic diagram of two-dimensional Fermi surfaces for the tetragonal phase. The contributions from three orbitals, $d_{xy}$, $d_{yz}$ and $d_{zx}$ are colored in blue, red, and green, respectively. Sufficiently expanded BFSs expected below $T_c$ are colored in purple [2,6].

In conclusion, we have observed the upturn of $1/T_1T$ deep in the SC state from $^{77}$Se-NMR measurements down to 100 mK. The upturn can be explained by the minimal two-band model, where the interband spin-triplet pairing is responsible for BFSs. The appearance of the upturn of $1/T_1T$ gives evidence for strong Bogoliubov quasiparticles interactions in addition to the presence of BFSs.


**References**

[1] C. Setty, S. Bhattacharyya, Y. Cao, A. Kreisel, and P. J. Hirshfeld, Nat. Commun. **11**, 523 (2020).
[2] Y. Cao, C. Setty, L. Fanfarillo, A. Kreisel, and P. J. Hirschfeld, Phys. Rev. B **108**, 224506 (2023).
[3] Z. Yu, K. Nakamura, K. Inomata, X. Shen, T. Mikuri, K. Matsuura, Y. Mizukami, S. Kasahara, Y. Matsuda, T. Shibauchi, Y. Uwatoko, and N. Fujiwara, Communications Physics **6** (2023) 175.
[4] T. Suzuki, A. Fukushima, S. Kasahara, K. Matsuura, M. Qiu, Y. Mizukami, K. Hashimoto, Y. Matsuda, T. Shibauchi, S. Shin, and K. Okazaki, https://doi.org/10.21203/rs.3.rs-2224728/v1.
[5] K. Matsuura, *et al.*, *PNAS* **120**, e2208276120 (2023).
[6] Y. Cao, C. Setty, A. Kreisel, L. Fanfarillo, and P. J. Hirschfeld, Phys. Rev. B **110**, L020503 (2024).



**Authors**

Z. Yu[a], K. Nakamura[a], K. Inomata[a], X. Shen, T. Mikuri, K. Matsuura[b], Y. Mizukami[b], S. Kasahara[c], Y. Matsuda[c], T. Shibauchi[b], Y. Uwatoko and N. Fujiwara[a],
[a]Kyoto University
[b]The University of Tokyo
[c]Kyoto University

PI of Joint-use project: N. Fujiwara
Host lab:Uwatoko Group


## Development of a Magnetic-Susceptibility-Measurement Apparatus Used under High Pressure in Pulsed High Magnetic Fields

The combination of extreme conditions such as low temperature, high magnetic field, and high pressure provide insights into electrical and magnetic physical properties in condensed-matter materials. To date, magnetization measurements have been reported with an induction method using a non-destructive pulse magnet and a metallic piston-cylinder cell (PCC) made by Cu-Be or Ni-Cr-Al alloy under high pressure of up to 0.95 GPa in pulsed high magnetic fields of up to 50 T [1-3]. In this method, magnetization signal was detected by winding pick-up coils with approximately 100 turns around the exterior of the PCC (left panel of Fig. 1). This measurement apparatus is an effective tool for observing large abrupt transition phenomena, but the following factors may interfere with accurate measurements: (a) low sample-filling rate inside the pick-up coil, (b) extrinsic magnetization signals from the pressure cell, and (c) Joule heating caused by eddy currents in the metallic parts of the pressure cell in pulsed high magnetic fields. To deal with these problems, we have designed a new

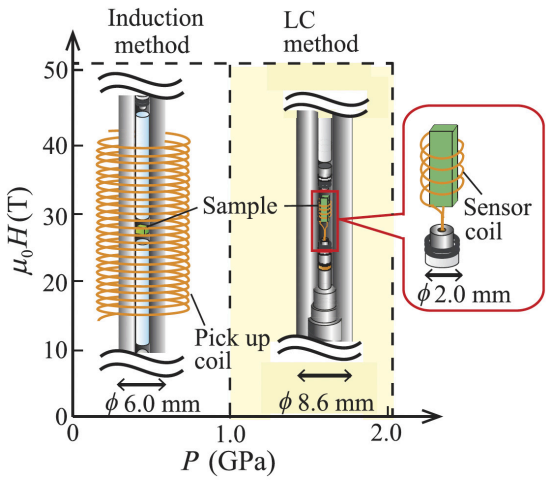


Fig. 1. Magnetic field and pressure range of magnetic-susceptibility-measurement techniques using the induction and LC methods. The schematic views below 1 GPa and above 1 GPa are the piston-cylinder cells around the sample for the induction and LC methods, respectively.

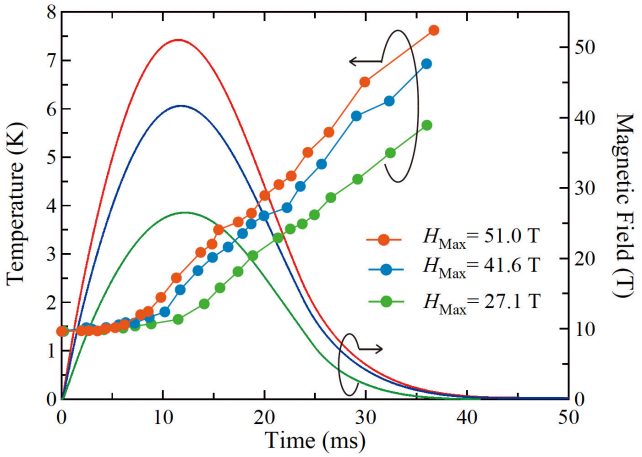


Fig. 2. Temperature change at the sample position inside the PCC starting at $T = 1.4$ K in various maximum magnetic fields. The red, blue and green lines with filled circles represent the temperature changes inside the PCC for the cases of $H_{Max} = 51.0$, 41.6, and 27.1 T, respectively.

PCC in use for pulsed high magnetic fields and developed a magnetic-susceptibility-measurement apparatus using a proximity detector oscillator (PDO) under high pressures in pulsed high magnetic fields [4].

The PDO is an inductance ($L$)-capacitance ($C$) self-resonating LC tank circuit based on a widely available proximity detector chip used in modern metal detectors [5,6]. When a magnetic insulator is put into the sensor coil, this circuit detects the change in the resonance frequency ($\Delta f$) corresponding to the change in the dynamic magnetic susceptibility (($\Delta M/\Delta H$). Hereafter, we refer to this technique as an LC method. The absolute value of $\Delta f$ increases as the sample filling rate increases against the sensor coil. The sensor coil is typically wound only 5–30 turns with a diameter as small as 300 μm. Therefore, the sensor coil including the sample can be inserted in the pressure cell as shown in the right panel of Fig. 1. This setting prevents the magnetization signal of the pressure cell from being superimposed to the measurement signal.

The PCC used in our magnetic-susceptibility measurements in pulsed high magnetic fields was made of Ni-Cr-Al alloy with a low conductivity and high tensile strength compared with a PCC made of Cu-Be alloy. The sensor coil is put into the PCC in this LC method, and therefore the outer diameter of the PCC can be expanded up to 8.6 mmφ, resulting in increasing the applied pressure of up to 2.10 ± 0.02 GPa.

To evaluate the effect on the Joule heating at the sample position in pulsed high magnetic fields, we investigated the temperature change in the sample space using a magnetic-field and temperature-calibrated thermometer. Figure 2 shows the temperature changes at the sample position inside the PCC, starting from an initial temperature of 1.4 K, in pulsed high magnetic fields as a function of time. For the maximum field of 51 T, the temperature at the sample position remained almost 1.4 K until nearly 6.5 ms (approximately 40 T during the field-ascending process). After approximately 6.5 ms, the temperature slowly increased, reaching approximately 8 K at 40 ms (around 0 T). Since the sample is covered with a Teflon tube and immersed in Daphne 7373 as a pressure medium, the Joule heating from the metallic parts of the PCC is transmitted to the sample position with some delay.

To verify the performance of our developed magnetic-susceptibility-measurement apparatus in pulsed high magnetic fields under high pressures, we investigated the pressure dependence of the magnetic susceptibility of $Ba_3CoSb_2O_9$, which is one of the typical $S = 1/2$ triangular lattice antiferromagnets and exhibits successive phase transitions below the Néel temperature $T_N = 3.8$ K [7]. Figure 3 shows the $\Delta f_{sub}$-$H$ curve of $Ba_3CoSb_2O_9$ for $H \parallel ab$ plane in pulsed magnetic fields of up to 51 T under pressures of up to 1.97 GPa. $\Delta f_{sub}$ is the frequency difference obtained by subtracting the frequency at $T = 10$ K as background from $\Delta f$ at 1.4 K. At ambient pressure in the PCC during the field-ascending process, $\Delta f_{sub}$-$H$ curve was in good agreement with the field derivative magnetization d$M$/d$H$ in a previous report [7]. Under several pressures, we also observed the anomalies at phase transition fields in the field-ascending process. In the field-descending process at ambient pressure in PCC and at 1.10 GPa, $\Delta f_{sub}$-$H$ curves did not show any anomalies at phase transition fields observed in the field-ascending process owing to the temperature increase of the sample above $T_N$. As aforementioned, $\Delta f_{sub}$ up to the saturation field ($H_{sat}$) of approximately 32 T in the field-ascending process (Fig. 3(a)) is not affected by the increase in the sample temperature due to Joule heating. The present study demonstrated that our developed magnetic-susceptibility-measurement apparatus is a powerful tool for investigating

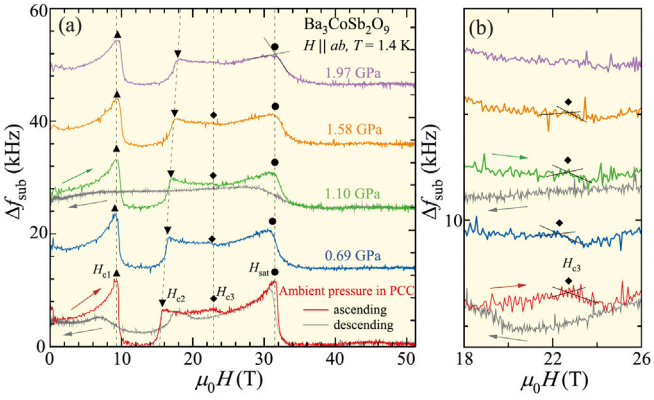


Fig. 3. (a) $\Delta f_{sub}$-$H$ curves for $H \| ab$ plane of $Ba_3CoSb_2O_9$ at 1.4 K at various pressures. Gray lines show $\Delta f_{sub}$-$H$ curves in the field-descending process at ambient pressure in PCC and at 1.10 GPa. Other lines are $\Delta f_{sub}$-$H$ curves in the field-ascending process. The dotted lines are guidelines indicating the pressure dependence of transition fields ($H_{c1}$, $H_{c2}$, $H_{c3}$ and $H_{sat}$). (b) Enlarged view of the $\Delta f_{sub}$-$H$ curves around 22 T. The curves in Figs. 3(a) and 3(b) are arbitrarily shifted from the ambient-pressure curve with increasing pressure for clarity.

magnetic properties of a frustrated magnet with a small spin value at low temperatures down to 1.4 K in pulsed high magnetic fields of up to 40 T under high pressures of up to 2.1 GPa. We hope that this apparatus will help us discover unconventional physical phenomena in quantum and frustrated spin systems.


**References**

[1] T. Hamamoto, K. Kindo, T. Kobayashi, Y. Uwatoko, S. Araki, R. Settai, and Y. Onuki, Physica B **281-282**, 64 (2000).
[2] T. Tahara, T. Kida, Y. Narumi, T. Takeuchi, H. Nakamura, K. Miyake, K. Kindo, and M. Hagiwara, J. Phys. Soc. Jpn. **89**, 064711 (2020).
[3] T. Matsunaga, T. Kida, S. Kimura, M. Hagiwara, S. Yoshida, I. Terasaki, and K. Kindo, J. Low Temp. Phys. **159**, 7 (2010).
[4] K. Nihongi, T. Kida, Y. Narumi, N. Kurita, H. Tanaka, Y. Uwatoko, K. Kindo, and M. Hagiwara, Rev. Sci. Instrum. **94**, 113903 (2023).
[5] M. M. Altarawneh, Ph.D. thesis, The Florida State University, 2009.
[6] S. Ghannadzadeh, M. Coak, I. Franke, P. A. Goddard, J. Singleton, and J. L. Manson, Rev. Sci. Instrum. **82**, 113902 (2011).
[7] T. Susuki, N. Kurita, T. Tanaka, H. Nojiri, A. Matsuo, K. Kindo, and H. Tanaka, Phys. Rev. Lett. **110**, 267201 (2013).



**Authors**

K. Nihongi[a], T. Kida[a], Y. Narumi[a], N. Kurita[b], H. Tanaka[b], Y. Uwatoko, K. Kindo, and M. Hagiwara[a]
[a]Osaka University
[b]Tokyo Institute of Technology

PI of Joint-use project: K. Nihongi
Host lab: Hagiwara, Kindo, and Uwatoko Groups


# Theoretically Predicted Collective Excitation Modes in the Quadruple-Q Magnetic Hedgehog Lattices

The Kondo-lattice magnets are recently attracting enormous research interest as hosts of rich topological magnetism. This class of magnets have localized spins coupled to itinerant electrons via exchange interactions, and the itinerant electrons mediate long-range RKKY-type interactions among the localized spins. A variety of topological magnetic textures, e.g., skyrmion crystals, meron crystals, hedgehog lattices, emerge as superpositions of multiple spin helices or spin-density waves with different wavevectors determined by the Fermi-surface nesting.

Recent intensive studies have rapidly clarified equilibrium phases and static properties of the Kondo-lattice magnets, and several new materials have been discovered and synthesized experimentally. However, their nonequilibrium properties and dynamical phenomena remain unclarified yet. Under these circumstances, we have started the research for their spin-charge dynamics and related phenomena based on large-scale numerical simulations using the supercomputer facilities in ISSP, University of Tokyo. Through these studies, we have revealed many interesting dynamical phenomena, e.g., microwave-induced magnetic topology switching [1], unexpected spin-charge segregation in the low-energy excitations of a zero-field skyrmion crystal phase [2], photoinduced magnetic phase transitions to 120-degree order [3], and peculiar collective excitation modes of hedgehog lattices [4].

Among them, the last one is the most recent achievement. Three-dimensional topological magnetic structures called magnetic hedgehog lattices (Figs. 1(a) and (b)) have been discovered recently in several itinerant magnets such as MnGe, $MnSi_{1-x}Ge_x$ and $SrFeO_3$. The research on magnetic hedgehog lattices to date has focused mainly on their properties at equilibrium. On the other hand, according to the fundamentals of electromagnetism, magnetic (anti)hedgehogs, which behave as emergent (anti)monopoles, should generate emergent electric fields when they move. Therefore, clarification of their excitation dynamics will directly lead to the discovery and exploration of new emergent phenomena and device functions of topological spin textures in dynamical regimes.

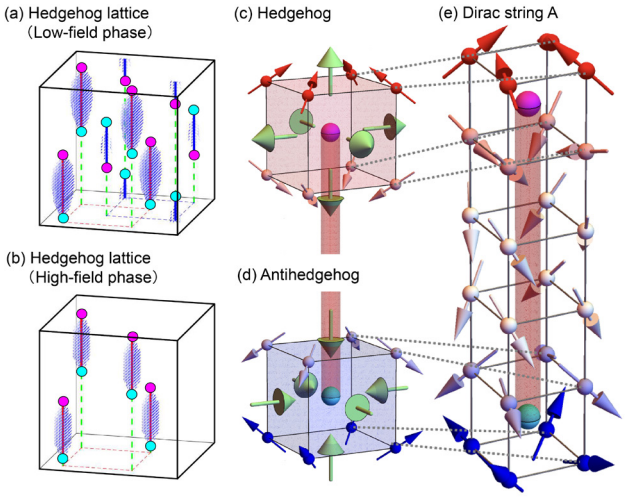


Fig. 1. (a), (b) Spatial arrangement of hedgehogs and antihedgehogs in magnetic hedgehog lattices. The magenta and cyan dots represent the hedgehogs and antihedgehogs, respectively. The lines connecting them represent Dirac strings. There are two types of Dirac strings (red line: Dirac string A, blue line: Dirac string B) with distinct magnetization winding senses. In the zero-field and low-field hedgehog lattice, both Dirac strings A and B exist (a). On the contrary, when the applied magnetic field exceeds a certain threshold value, the Dirac strings B disappear, and a hedgehog lattice with only Dirac strings A appears (b). (c), (d) Magnetization configurations (red and blue arrows) and distributions of emergent magnetic fields (green arrows) for a hedgehog and an antihedgehog. The hedgehog behaves as a source of the emergent magnetic fields, while the antihedgehog behaves as a sink of the fields. (e) Magnetization configuration of the magnetic vortex (Dirac string A) connecting the hedgehog and antihedgehog.

Motivated by this aspect, we investigated the nature and properties of collective excitation modes expected when the quadratic-$Q$ hedgehog lattices realized in $MnSi_{1-x}Ge_x$ and $SrFeO_3$ are irradiated by light by means of numerical simulations using a microscopic theoretical model. In the magnetic hedgehog lattices, hedgehogs (Fig. 1(c)) and antihedgehogs (Fig. 1(d)) are connected by a magnetic vortex called Dirac string (Fig. 1(e)). As shown in Fig. 1(e), the spins below the magnetic hedgehog go rotating down to the antihedgehog to form a vortex structure connecting the hedgehog and the antihedgehog. Because the rotating sense of the vortex is two-fold, there are two types of Dirac strings, which are right-handed and left-handed. Although two types of Dirac strings do not necessarily appear in a single material, in the case of the hedgehog lattices realized in $MnSi_{1-x}Ge_x$, there are indeed two types of Dirac strings (A and B) with different winding senses.

In the theoretical work reported in Ref. [4], we discovered that there exist three collective excitation modes (spin-wave modes) in terahertz to sub-terahertz frequency regime, which we named L1, L2 and L3 modes (Figs. 2(a) and (b)). Further analyses revealed that for the L2 and L3 modes, in-phase oscillations of the hedgehog and antihedgehog located at upper and lower ends of the Dirac string occur to exhibit translational oscillation, that is, the Dirac strings move upwards and downwards in an oscillatory manner (Figs. 2(c) and (d)). It is well-know that when a bar magnet is moved closer to or further away from a metallic coil, an

electric voltage is generated. It is interesting that the collective translational oscillations of the Dirac strings discovered here are the equivalent motion as that of the bar magnet in this case. In other words, in light-irradiated magnetic hedgehog lattices, a huge number of nano-sized bar magnets show such oscillatory motion at high frequencies of terahertz or sub-terahertz orders.

More interestingly, among the three oscillation modes, we found that the L2 mode corresponds to the oscillations of the Dirac strings B (Fig. 2(c)), while the L3 mode corresponds to those of the Dirac strings A (Fig. 2(d)). Consequently, we expect that the L2 (L3) mode vanishes when the Dirac strings B (A) disappear. In fact, application of a magnetic field can realize the selective disappearance of the Dirac strings B through inducing hedgehog-antihedgehog pair annihilations (Figs. 1(a) and (b)). We indeed observed that the L2 mode vanishes upon this field-induced annihilation of the Dirac strings B as seen in Fig. 2(b). This means that the external magnetic field can switch these collective oscillation modes, which enables us to realize on-off of the emergent electric fields and transmission of microwaves at corresponding frequencies.

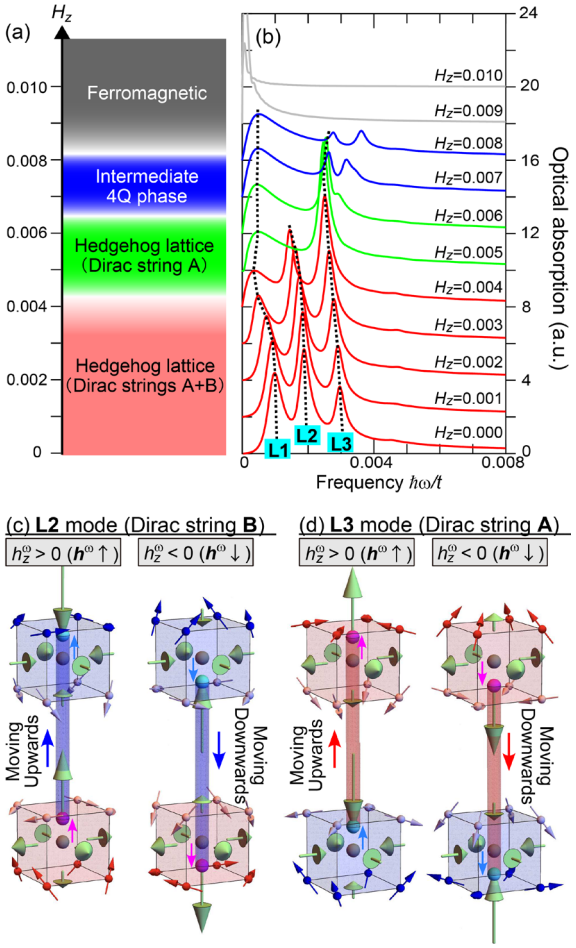


Fig. 2. (a) Phase diagram as a function of the external magnetic field $H_z$. At zero and low magnetic field, a hedgehog lattice with both Dirac strings A and B appears. As the magnetic field is increased, the hedgehog and antihedgehog belonging to the Dirac string B annihilate, and a phase transition occurs to a hedgehog lattice consisting of only the Dirac strings A. (b) Calculated optical absorption spectra. Three peaks correspond to collective excitation modes (named L1, L2, and L3) at the eigenfrequencies. The values of frequencies are written in normalized units, and these modes appear in a frequency range of approximately several hundred gigahertz or sub-terahertz. Looking at the L2 and L3 modes corresponding to the Dirac-string oscillations, both L2 and L3 modes appear in the low-field hedgehog-lattice phase where both Dirac strings A and B exist. On the contrary, in the high-field hedgehog-lattice phase without Dirac strings B, the L2 mode originating from the Dirac strings B disappears and only the L3 mode originating from the Dirac strings A remains. (c) Translational oscillations of the Dirac string B in the L2 mode. (d) Those of the Dirac string A in the L3 mode. The hedgehog and antihedgehog at the upper and lower ends of the string exhibit in-phase oscillations, which cause vertically translational oscillations of the strings.

Our discovery of the collective excitation modes of emergent magnetic (anti)monopoles in condensed matters is of importance from the viewpoint of fundamental science. Moreover, the discovery is expected to open the way to designing the optical/microwave device functions and spintronics functions of the three-dimensional topological magnetism that can be controlled and switched by external fields.

**References**
[1] R. Eto and M. Mochizuki, Phys. Rev. B **104**, 104425 (2021).
[2] R. Eto, R. Pohle, and M. Mochizuki, Phys. Rev. Lett. **129**, 017201 (2022).
[3] T. Inoue and M. Mochizuki, Phys. Rev. B **105**, 144422 (2022).
[4] R. Eto and M. Mochizuki, Phys. Rev. Lett. **132**, 226705 (2024).

**Authors**
M. Mochizuki[a]
[a]Waseda University

PI of Joint-use project: M. Mochizuki
Host lab: Supercomputer Center

## Odd-Parity Multipole Order in the Spin-Orbit Coupled Metallic Pyrochlore $Pb_2Re_2O_{7-\delta}$

Transition metal compounds containing 4*d* and 5*d* electrons have attracted attention for their novel physical properties resulting from their strong spin–orbit interaction (SOI) [1,2]. L. Fu pointed out that SOI induces Fermi-liquid instability in metals, leading to the formation of various electronic phases, and proposed the concept of spin-orbit-coupled metals (SOCM) [3]. In SOCM, the strong SOI induces a structural phase transition with spontaneous spatial-inversion-symmetry breaking (ISB), which is associated with an unconventional odd-parity multipole ordering [4]. To date, the candidate compounds of SOCM are limited and only few of them have been experimentally verified. Progress in material development is key to reveal the diversity of electronic orders formed in SOCM and further scrutinize the physics of SOCM.

So far, many studies have focused on α-pyrochlore oxide $Cd_2Re_2O_7$ (CRO), the most investigated candidate for SOCM [4]. Three successive structural phase transitions occur in CRO; an ISB transition from the regular pyrochlore structure (phase I) to the tetragonal phase II occurs at $T_{s1}$; on further cooling, transitions to an orthorhombic phase XI at $T_{s2}$ and to the tetragonal phase III at $T_{s3}$ occur. A theoretical work suggests that, in the phases II and III, the electronic order associated with ISB can be described by an odd-parity multipole order [3]. As depicted in Fig. 1, the displacements of Re atoms in phase II and III can be viewed as electric dipoles, certain pairs of which generate electric toroidal moments. These virtual electric toroidal moments are organized as $x^2 - y^2$ and $3z^2 - r^2$ configurations, respectively. Thus, the emerged electronic orders are regarded as electric toroidal quadrupole (ETQ) orders [2]. This unconventional odd-parity multipole ordering will induce ETQ-driven phenomena, such as the spin-split Fermi surface, the magneto-current effect, and nonreciprocal transport in an

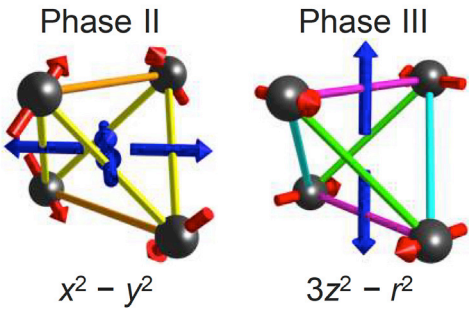


Fig. 1. Schematic figure of the deformation of Re tetrahedron in phases II and III of $Cd_2Re_2O_7$ (CRO), with red arrows representing the displacements of Re atoms (black balls). The Re displacements generate virtual electric toroidal moments (blue arrows) of the $x^2 - y^2$ and $3z^2 - r^2$ types, respectively. The colors of the connecting rods between Re atoms differentiate identical bonds in each phase.

applied magnetic field.

The relevant rhenium-containing pyrochlore oxide, $Pb_2Re_2O_{7-\delta}$ (PRO), has also been reported to exhibit an ISB phase transition from the α-pyrochlore structure (phase I) to a noncentrosymmetric structure (phase II) at $T_s = 300$ K [5,6]. Based on the ISB transition and similarity in the physical properties with CRO, PRO likely to be a SOCM. Therefore, an odd-parity multipole order may be realized. However, the crystal structure of phase II, which is crucial to identify the multipole order, is contradicting; two different structures, a cubic $F4\text{-}3m$ and a tetragonal $I\text{-}4m2$ structures are proposed [5,6]. Both crystal structures differ from that of CRO in the lowest temperature phase, which suggest a different multipole order is formed in PRO.

In this study, we investigated the low temperature phase of a SOCM candidate PRO by temperature-dependent synchrotron x-ray diffraction (XRD) measurements using single crystals [7]. As shown in Fig. 2, the appearance of superlattice peaks in the diffraction data of phase II indicates the violation of the *d*-glide plane derived extinction rule. To obtain more evidence for a lower crystal symmetry, we probed the temperature dependence of the two Bragg reflections (18 0 0) and (20 0 0) in phase I, as shown in Fig. 2 (c). Below $T_s$, the (18 0 0) reflection emerges upon cooling, indicating structural transition at $T_s$. In addition, the (20 0 0) reflection splits into two peaks (a low-angle and a high-angle peaks at an intensity ratio of approximately 2:1) demonstrating a cubic to tetragonal transition. It is noted that the (18 0 0) reflection is a single peak, not a double peak like the (20 0 0) reflection, demonstrating the presence of an additional extinction rule in phase II.

Since the phase transition at $T_s$ is of second order, the group-subgroup relation of the space group is applied to deduce the space group of phase II. Based on the observed reflection conditions, we propose the $I4_122$ space group for the phase II. This space group is identical to that of CRO in phase III.

The electronic order emerging in phase III of CRO is considered to be ETQ order with $3z^2 - r^2$ component. Since the lowest temperature structure of CRO and PRO is revealed to be identical, $3z^2 - r^2$-type ETQ is likely formed in the phase II of PRO. Here, $3z^2 - r^2$-type order is selected as the ground state from the doubly degenerate $x^2 - y^2$ and $3z^2 - r^2$-type ETQ orders. Electronic details about the origin of this symmetry breaking are of interest for future studies. Further comparison of the ISBs with respect to their origin and final manifestation in CRO and PRO would be useful for fundamental understanding of SOCM.

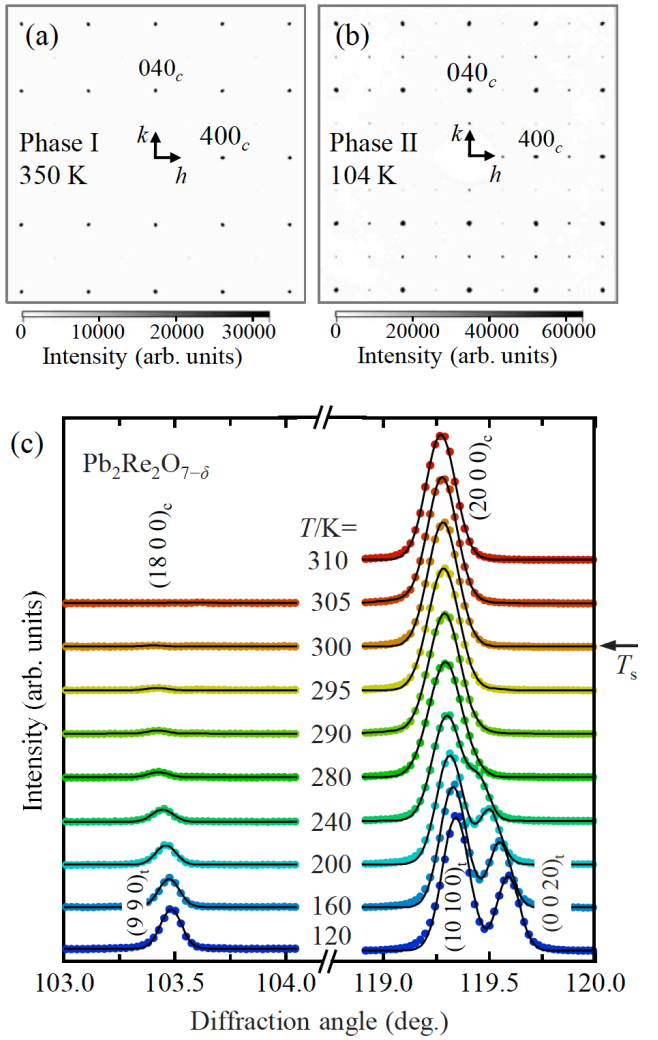


Fig. 2. Diffraction data of the $hk0$ plane for $Pb_2Re_2O_{7-\delta}$ (PRO) in (a) phase I and (b) II. The appearance of superlattice peaks in (b) indicates the violation of the *d*-glide plane derived extinction rule. (c) . Temperature variation of XRD patterns near the (20 0 0) and (18 0 0) reflections of PRO. Solid black lines represent fitting curve. The transition temperature $T_s = 300$ K is marked with an arrow.


**References**

[1] T. Takayama, J. Chaloupka, A. Smerald, G. Khaliullin, and H. Takagi, J. Phys. Soc. Japan **90**, 062001 (2021).
[2] L. Fu, Phys. Rev. Lett. **115**, 026401 (2015).
[3] S. Hayami, Y. Yanagi, H. Kusunose, and Y. Motome, Phys. Rev. Lett. **122**, 147602 (2019).
[4] Z. Hiroi, J.-I. Yamaura, T. C. Kobayashi, Y. Matsubayashi, and D. Hirai, J. Phys. Soc. Japan **87**, 024702 (2018).
[5] K. Ohgushi, J. I. Yamaura, M. Ichihara, Y. Kiuchi, T. Tayama, T. Sakakibara, H. Gotou, T. Yagi, and Y. Ueda, Phys. Rev. B **83**, 125103 (2011).
[6] C. Michioka, Y. Kataoka, H. Ohta, and K. Yoshimura, J. Phys. Condens. Matter **23**, 445602 (2011).
[7] Y. Nakayama, D. Hirai, H. Sagayama, K. Kojima, N. Katayama, J. Lehmann, Z. Wang, N. Ogawa, and K. Takenaka, Phys. Rev. Mater. **8**, 055001 (2024).



**Authors**

Y. Nakayama[a], D. Hirai[a], H. Sagayama[b], K. Kojima[a], N. Katayama[a], J. Lehmann[c], Z. Wang[c], N. Ogawa[c], and K. Takenaka[a]
[a]Nagoya University
[b]KEK, [c]RIKEN

PI of Joint-use project: D. Hirai
Host lab: Hiroi and Okamoto Groups

# New Intermetallic Compounds in Sm-Fe System Alloys

High-performance neodymium-iron-boron (Nd-Fe-B) magnets are applied to various advanced electromagnetic devices, including hard disk drives, electric vehicles, and medical equipment [1]. In particular, the production of electric cars equipped with Nd-Fe-B magnet motors has significantly increased, reflecting that regulations on internal combustion engines emitting large quantities of greenhouse gases have been proposed or enacted in many countries. The continuously growing demand for high-performance Nd-Fe-B magnets has raised severe concerns over their price and availability [2]. Under such circumstances, the development of permanent magnets using the relatively abundant rare-earth element Sm has become a focus of attention. Therefore, we have continued searching for new Sm-based rare-earth intermetallic compounds.

This study chose Sm-Fe system alloys as new Sm-based rare-earth intermetallic compounds. Although only three intermetallic compounds, $Sm_2Fe_{17}$, $SmFe_3$, and $SmFe_2$ phases are found in the Sm-Fe phase diagram [3], the formation of new intermetallic compounds, such as $SmFe_{12}$, $SmFe_5$, and $Sm_5Fe_{17}$ phases, has been reported in thin film processing [4-6]. It is necessary to obtain these materials in bulk form to evaluate the magnetic properties of these phases. This study investigates the possibility of producing these new intermetallic compounds through rapid solidification processing using a melt-spinning technique. The structures and magnetic properties of the melt-spun ribbons were investigated.

Since the new intermetallic compounds are metastable, it is impossible to produce alloys with these phases using the conventional casting method. Thus, the specimens were prepared by rapid solidification processing using melt-spinning. Figure 1 shows the transmission electron microscope (TEM) micrograph of the as-quenched $SmFe_5$ melt-spun ribbon and the corresponding selected electron diffraction pattern. The electron diffraction pattern indicates that the fine grains in the TEM micrograph were in the $SmFe_5$ phase. This confirms that the as-quenched $SmFe_5$ melt-spun ribbon consisted of $SmFe_5$ fine grains. Heat treatment of the as-quenched melt-spun ribbon resulted in crystal growth of the $SmFe_5$ grains [7]. On the other hand, the $SmFe_{12}$ and $Sm_5Fe_{17}$ phases were not obtained by rapid solidification processing using melt-spinning. These as-quenched melt-spun ribbons were amorphous. Although the $Sm_5Fe_{17}$ phase was produced by melt-spinning followed by optimal heat treatment, the $SmFe_{12}$ phase was not obtained by annealing the $SmFe_{12}$ melt-spun ribbon. The $SmFe_{12}$ phase was found to be obtained by adding small elements, such as Ti or V, to the $SmFe_{12}$ phase.

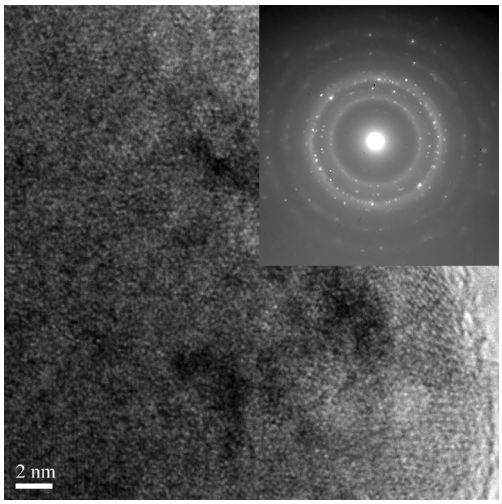


Fig. 1. TEM micrograph of the as-quenched $SmFe_5$ melt-spun ribbon and the corresponding selected electron diffraction pattern.

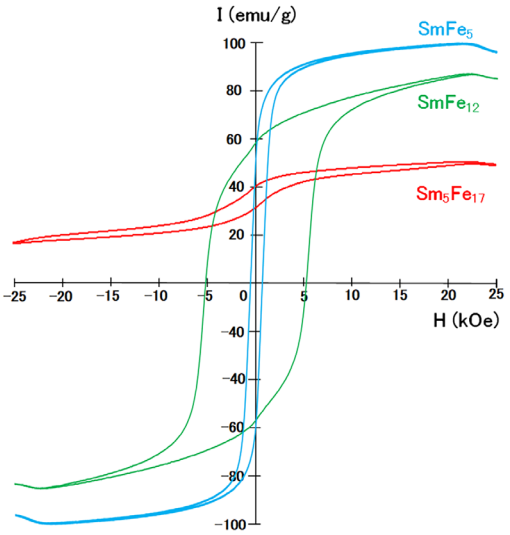


Fig. 2. Hysteresis loops of $SmFe_{12}$, $SmFe_5$, and $Sm_5Fe_{17}$ melt-spun ribbons. The hysteresis loops were measured by VSM with a maximum applied magnetic field of 25 kOe.

The magnetic properties of the new intermetallic compounds were evaluated by the vibrating sample magnetometer (VSM). Figure 2 shows the typical magnetic hysteresis loops of these phases. These new intermetallic compounds exhibited hysteresis loops as magnetic materials. The $SmFe_5$ melt-spun ribbon showed a narrow hysteresis loop with moderate coercivity, and the $SmFe_{12}$ melt-spun ribbon showed a wide hysteresis loop with high coercivity. On the other hand, the $Sm_5Fe_{17}$ melt-spun ribbon exhibited a minor loop, not a hysteresis loop. The coercivity of the $Sm_5Fe_{17}$ melt-spun ribbon was extremely high, over the applied field of 25 kOe in the VSM measurement, and only the minor loop was obtained in the $Sm_5Fe_{17}$ melt-spun ribbon.

This study obtained the new intermetallic compounds of the $SmFe_{12}$, $SmFe_5$, and $Sm_5Fe_{17}$ phases. However, the magnetic properties of these compounds are not yet comparable to those of high-performance Nd-Fe-B magnets. Further optimization of the annealing conditions and compositional modifications may improve the magnetization of these new intermetallic compounds.

**References**

[1] G. Bailey, N. Mancheri, and K. V. Acker, J. Sustain. Metall. **3**, 611 (2017).
[2] T. Dutta, K. H. Kim, M. Uchimiya, E. E. Kwon, B. H. Jeon, A. Deep, and S. T. Yun, Environ. Res. **150**, 182 (2016).
[3] K. H. J. Busschow, J. Less-Common Met. **25**, 131 (1971).
[4] F. J. Cadieu, H. Hegde, R. Rani, A. Navarathna, and K. Chen, Mater. Lett. **11**, 284 (1991).
[5] P. Tozmana, H. Sepehri-Amina, and K. Hono, Scripta Mater. **194**, 113686 (2021).
[6] O. Yabuhara, M. Ohtake, Y. Nukaga, F. Kirino, and M. Futamoto, J. Phys.: Conf. Ser. **200**, 082026 (2010).
[7] T. Saito and D. Nishio-Hamane, AIP Advances **10**,015311 (2020).

**Authors**
T. Saito[a] and D. Nishio-Hamane
[a]Chiba Institute of Technology

PI of Joint-use project: T. Saito
Host lab: Electron Microscope Section

# Structural Study of Perovskite-type $RbNbO_3$ Prepared at High Pressure

We successfully synthesized a perovskite-type $RbNbO_3$ compound by subjecting the non-perovskite $RbNbO_3$ [1,2] to high temperature (1173 K) and high pressure (4 GPa) using a cubic-type high-pressure press. We investigated the temperature dependence of crystal structure associated with dielectric properties. Base on the powder X-ray diffraction patterns collected at ISSP under the collaborative program, we determined lattice parameters of the temperature dependence of perovskite $RbNbO_3$ at 4–300 K. Our objective in this project is to discover novel ferroelectrics that are equal to or beyond $BaTiO_3$, which is often utilized in a range of electrical devices. $KNbO_3$ is a widely recognized displacement-type ferroelectric material, and we aimed to replace the potassium (K) ion with rubidium (Rb) ion, which belong to the same group of alkali metals but have a greater ionic radius. $RbNbO_3$ has a complex quasi one-dimensional structure under normal conditions, unlike the perovskite-type structure found in $KNbO_3$. We synthesized $RbNbO_3$ with the perovskite structure using the high pressure technique. Detailed study was published in the reference [2].

The high-pressure phase of $RbNbO_3$ at 300 K was found to have an orthorhombic cell with a perovskite-type structure. The crystal structure was determined by single-crystal X-ray diffraction analysis at Tohoku University. The space group was identified as *Amm2*, with a lattice parameter of $a = 3.9937(2)$ Å, $b = 5.8217(3)$ Å, and $c = 5.8647(2)$ Å. The non-centrosymmetric space group of $RbNbO_3$ is same as that of the ferroelectric compounds $BaTiO_3$ and $KNbO_3$. The degree of distortion in $RbNbO_3$ is more pronounced than in $KNbO_3$, perhaps because of the larger ionic radius of Rb. The transitions from an orthorhombic structure to two sequential tetragonal phases (Tetra1 at 493 K, Tetra2 at 573 K) were observed. The perovskite framework was maintained during both phases before returning to the triclinic ambient phase at 693 K, as seen in Fig. 1. The first transition is similar to that observed in $KNbO_3$, however the subsequent transition from the Tetra1 phase to the Tetra2 phase is distinct, characterized by elongation along the *c*-axis and a notable increase in the $c_p/a_p$ ratio ($c_p$ and $a_p$ are taken with perovskite basic cell) from 1.07 to 1.43. This distortion indicates a transition that is comparable to the one observed in $PbVO_3$ [3], where the oxygen atoms of an octahedron move apart along the *c*-axis, resulting in the formation of a pyramid as shown in Fig. 1. The permittivity exhibits a

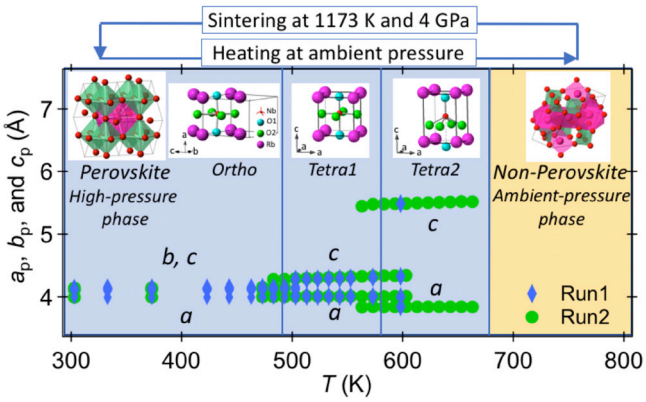


Fig. 1. Temperature dependence of crystal structure of $RbNbO_3$ at 300–800 K [2]. The lattice parameters, $a_p$, $b_p$ and $c_p$, are taken with perovskite basic cell. The figure was reprinted from the graphical index of Ref. 2 published by the Royal Society of Chemistry.

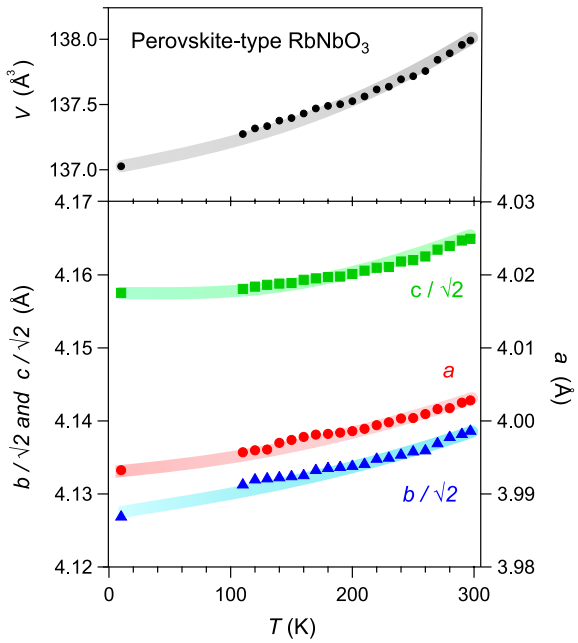


Fig. 2. Temperature dependence of lattice parameters of perovskite-type $RbNbO_3$ at 4–300 K.

discontinuous increase at the orthorhombic to tetragonal phase transition, however this enhancement is not observed for the Tetra1 and Tetra2 transitions due to the collapse of the bulk sample caused by abrupt volume expansion during the transition.

There were no observable alterations in the structure between temperatures of 4 and 300 K. The lattice parameters, *a*, *b*, *c*, and *V* exhibited consistent decreases with decreasing temperature, as seen in Fig. 2. A contrasting structural phase shift from orthorhombic to rhombohedral occurs at 220 K in $KNbO_3$. This aligns with the findings reported by Fukuda *et al*. [1]. Nevertheless, the theoretical calculations regarding phase stability indicate that the orthorhombic structure with *Amm*2 is the most stable phase in $RbNbO_3$, exhibiting the lowest energy [2]. It is contrast to that the stable space group in $KNbO_3$ at low temperature is *R3m*.

In addition, we conducted thermal property measurements using a combination of thermogravimetry (TG), differential thermal analysis (DTA), and differential scanning calorimetry (DSC). Furthermore, we assessed the optical characteristics using second harmonic generation (SHG) [2]. We further synthesize a solid solution of $RbNbO_3$ and $KNbO_3$ by using the high pressure method, and investigate the structural studies with wide range of temperature. Ongoing research involves doing structural studies at various temperatures.

**References**


[1] M. Fukuda and K. Yamaura, J. Ceram. Soc. Jpn. **131**, 126 (2023).
[2] A. Yamamoto, K. Murase, J. Yamaura, *et al*. Dalton Trans. **53**, 7044 (2024).
[3] R. V. Shpanchenko *et al*., Chem. Mater. **16**, 3267 (2004).



**Authors**
A. Yamamoto[a], K. Murase[a], J. Yamaura, K. Sugiyam[b], and T. Kawamata[b]
[a]Shibaura-Institute of Technology
[b]Tohoku University

PI of Joint-use project: Ayako Yamamoto
Host lab: Yamaura group and X-Ray Diffraction Section

# Implementation of Finite-Temperature Calculation in TeNeS

In quantum many-body problems, such as quantum spin systems and strongly correlated electron systems, the dimension of the Hilbert space increases exponentially with the number of spins or particles, making precise analysis of large systems difficult. The tensor network method, which is one technique to overcome such difficulties, represents quantum states as a network constructed by the contraction of small tensors, thereby reducing the effective degrees of freedom and enabling the computation of large systems. The infinite projected entangled pair state/infinite tensor product states (iPEPS/iTPS) is a tensor network that can directly represent the ground state of an infinitely large system. We are developing a tensor network library Tensor Network Solver (TeNeS) based on iPEPS/iTPS[1, 2]. TeNeS supports MPI and OpenMP hybrid parallelization, and enables us to calculate the ground states of various two-dimensional lattice models.

This year, through the support of Project for Advancement of Software Usability in Materials Science (PASUMS), we have implemented the finite-temperature calculation in TeNeS. The finite-temperature calculation is essential for the analysis of the physical properties of quantum many-body systems, such as the specific heat, and magnetization. The finite-temperature calculation is performed by the imaginary time evolution of the density matrix represented by the infinite projected entangled pair operator/infinite tensor product operator (iPEPO/iTPO) [3] (See Fig. 1). Such imaginary time evolution for iPEPO/iTPO is algorithmically similar to the ground state calculation based on iPEPS/iTPS, and we can easily implement the finite-temperature calculation in TeNeS.

In addition to the finite-temperature calculation, we also implemented the real-time evolution of a pure state using TeNeS. The algorithm of the real-time evolution is essentially the same as the imaginary time evolution. However, usually approximation based on iPEPS/iTPS becomes less accurate for longer time evolution due to the increase of quantum entanglement. Thus, real-time evolution approximated by iPEPS/iTPS is limited to short time evolution.

The finite-temperature calculation and the real-time evolution implemented in TeNeS are useful for the analysis of the physical properties of quantum many-body systems. We hope that TeNeS can enhance research in the field of quantum many-body systems.

TeNeS was developed with Yuichi Motoyama, Kazuyoshi Yoshimi, Satoshi Morita, Tatsumi Aoyama, Takeo Kato, and Naoki Kawashima.

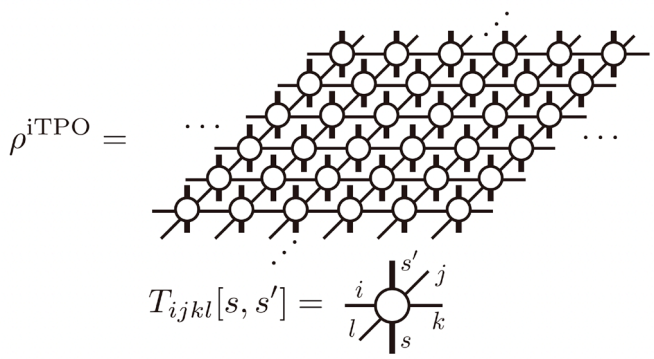


Fig. 1. Tensor network diagram of a density matrix ρ represented as an iPEPO/iTPO. Vertical open legs stand for indices of local Hilbert space.


**References**

[1] Y. Motoyama, T. Okubo, K. Yoshimi, S. Morita, T. Kato, and N. Kawashima, Comput. Phys. Commun. **279**, 108437 (2022).
[2] https://github.com/issp-center-dev/TeNeS
[3] A. Kshetrimayum, M. Rizzi, J. Eisert, and R. Oru´s, Phys. Rev. Lett. **122** 070502(2019).



**Author**

T. OKUBO[a]
[a]Institute for Physics of Intelligence, the University of Tokyo

PI of Joint-use project: T. Okubo
Host lab: Supercomputer Center


# Magnetic Field Induced Insulator-to-Metal Mott Transition in λ-Type Organic Conductors

The Mott transition is a key issue in condensed matter physics. Mott transitions give rise to novel physical phenomena, including unconventional superconductivity and quantum criticality. The interest in this research is the effects of the magnetic field on the Mott transition. To thoroughly investigate the effects of the magnetic field on the Mott transition, it is necessary to apply a magnetic field comparable to the energy scale of the Mott gap. However, the energy scale of the Mott gap is usually much larger than the practical limits of experimentally feasible magnetic fields. To avoid this problem, it is necessary to prepare materials near the Mott boundary region to reduce the Mott gap.

For studying the magnetic field effects on the Mott transition, we focused on λ-type organic conductors. Figure 1 shows the pressure-temperature ($p$ - $T$) phase diagram of λ-type BETS salts λ-$(BETS)_2GaBr_xCl_{4-x}$, where BETS is bis(ethylenedithio)tetraselenafulvalene. It has been reported that the increase in Br content works as a negative pressure effect and that the compound with $x \sim 0.75$ is located near the Mott boundary [1]. These indicate that by controlling the Br content $x$, we can access the Mott boundary region under ambient conditions, which allows us to study the magnetic field effects on the Mott transition over a wide temperature and magnetic field ranges using pulsed magnetic fields.

In this study, we performed magnetoresistance measure-

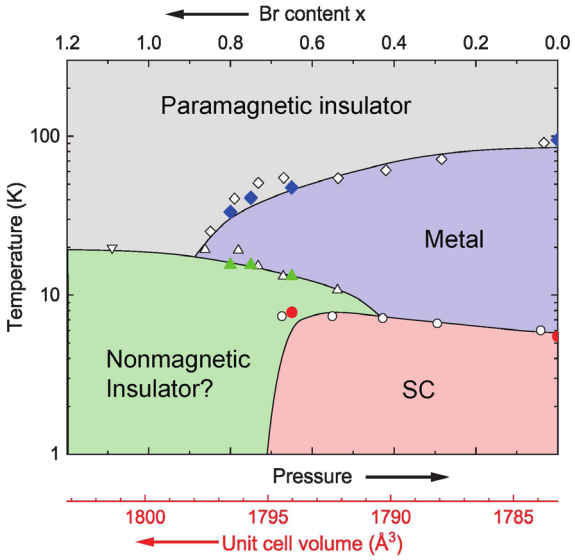


Fig. 1. $p$ - $T$ phase diagram of λ-$(BETS)_2GaBr_xCl_{4-x}$. The red horizontal axis indicates the unit cell volume at room temperature [1]. The points marked with blue diamonds, green triangles, and red circles were determined in this study.

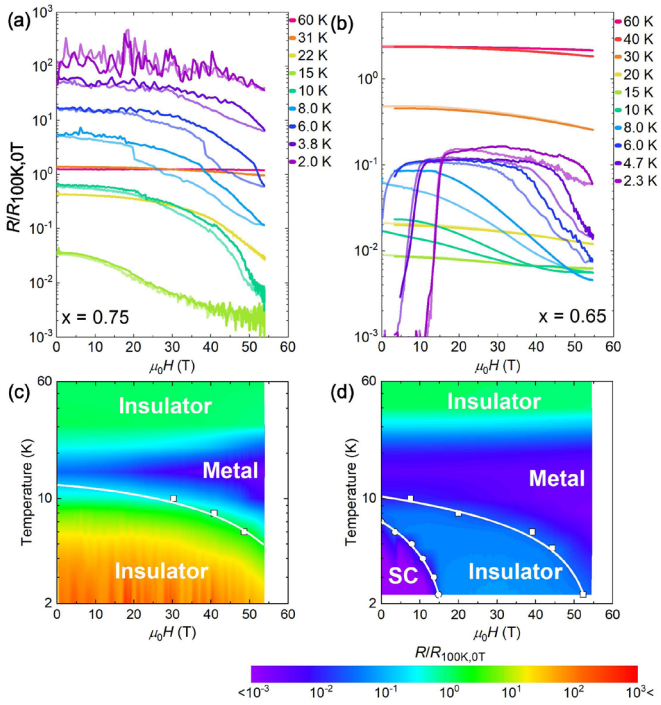


Fig. 2. (a), (b) Magnetic field dependence of the resistivity of the compound with $x = 0.75$ and 0.65. (c), (d) $H$ - $T$ phase diagram of the compound with $x = 0.75$ and 0.65.

ments using a 60 T pulse magnet at the International MegaGauss Science Laboratory. We synthesized λ-type organic conductors with $x = 0.65$, 0.75, and 0.8, which are located near the Mott boundary. Figures 2 (a) and 2(b) show the temperature dependence of the magnetoresistance for compounds with $x = 0.75$ and 0.65 [2]. We confirmed that in the compound with $x = 0.75$, a sharp drop with hysteresis in resistivity was observed at a certain magnetic field, suggesting that a first-order magnetic field induced insulator-to-metal Mott transition occurs. Interestingly, in the compound with $x = 0.65$, the suppression of the superconducting state at low magnetic fields and a Mott transition at high magnetic fields were observed, indicating a successive superconductor-to-insulator-to-metal transition. These results are summarized as a color plot of the field-temperature ($H$ - $T$) phase diagram shown in Figs. 2 (c) and 2(d). We note that the magnetic field induced Mott transition observed previously in κ-type organic conductors is a transition from the metallic to the insulating state by applying a magnetic field, whereas the Mott transition observed in λ-type salts in this study is a transition from the insulating to the metallic state, that is, the opposite magnetic field response was observed [3].

We proposed that the difference in magnetic susceptibility between the insulating and metallic phases across the Mott boundary is key to explaining the opposite magnetic field effects on the Mott transition. The previous studies reported that the magnetic susceptibility of λ-$(BETS)_2GaBr_xCl_{4-x}$ decreases with increasing Br content at low temperatures [2]. This suggests that the magnetization of the metal phase is larger than that of the insulator phase. Since the spin state with larger magnetization is more stabilized under magnetic fields, the metallic state is stabilized in magnetic fields.

In this study, we have experimentally verified a magnetic-field-induced insulator-to-metal Mott transition and a successive superconductor-to-insulator-to-metal transition from magnetoresistance measurements for λ-type organic Mott insulators. These experimental results not only provide new insight into the magnetic field effects on the Mott transition but also highlight that the Mott transition can be induced in experimentally feasible magnetic fields at ambient pressure conditions through the control of chemical pressure in λ-type organic conductors, thereby paving the way for future microscopic investigations of the field-induced Mott transition.

**References**
[1] H. Tanaka, A. Kobayashi, A. Sato, H. Akutsu, and H. Kobayashi, J. Am. Chem. Soc. **121**, 760(1999).
[2] S. Fukuoka, T. Oka, Y. Ihara, A. Kawamoto, S. Imajo, and K. Kindo, Phys. Rev. B **109**, 195142 (2024).
[3] F. Kagawa, T. Itou, K. Miyagawa, and K. Kanoda, Phys. Rev. Lett. **93**, 127001 (2004).

**Authors**
S. Fukuoka[a], T. Oka[a], Y. Ihara[a], A. Kawamoto[a], S. Imajo, and K. Kindo
[a]Hokkaido University

PI of Joint-use project: S. Fukuoka
Host lab: Kindo Group

## Search for Valence and Structural Transition in Eu Alloy in Magnetic Field

The 122-type intermetallic compound $Eu_x(Co_{1-x}Ni_x)_2P_2$ shows a correlation between multiple degrees of freedom in the solid resulting in various phenomena such as isostructural transition between the collapsed tetragonal (cT) and uncollapsed tetragonal (ucT) structures, 3$d$ magnetism, and the formation of P-P dimers. To gain insights on the correlated behavior and to search for magnetic-field-induced phase transitions, we investigate the effect of high magnetic fields on the samples of $x = 0.4$ and 0.5. As the samples are in the Eu valence fluctuating regime, the structural phase transition from cT to ucT may be induced by the Eu valence change under the strong magnetic fields. We have performed the magnetostriction and magnetization measurements up to 60 T in the pulsed high field generated at the IMGSL in ISSP.

Figure shows the magnetic field dependence of the magnetostriction and magnetization of the sample of $x = 0.4$. The magnetostriction smoothly increases with increasing magnetic fields. The behavior is in good agreement with the calculated results using the inter-configurational fluctuation model that describes the Eu valence change. This indicates that magnetostriction represents the change of the Eu valence state in the compound. The magnetization curve also shows relatively good agreement with the model at high magnetic fields. In contrast, in the low-magnetic-field region below 20 T, magnetization curves do not agree with the model. The anomalies in the magnetization at around 10 and 15 T are likely attributed to the spin-flop transitions of the 3$d$ electrons. These results indicate that the changes in the Eu valence manifest themselves in the magnetization curves at high magnetic fields, while the magnetism of the 3$d$ electrons manifests itself in the magnetization at low magnetic fields. We conclude that the valence change occurs within the Eu valence fluctuation regime coupled with the cT structure.

The absence of the abrupt changes in the magnetostriction should indicate that the transition to ucT structure, which is firmly coupled with the divalent Eu state, does not occur within the magnetic field range of the present study. Even higher magnetic fields or pulsed magnetic fields with

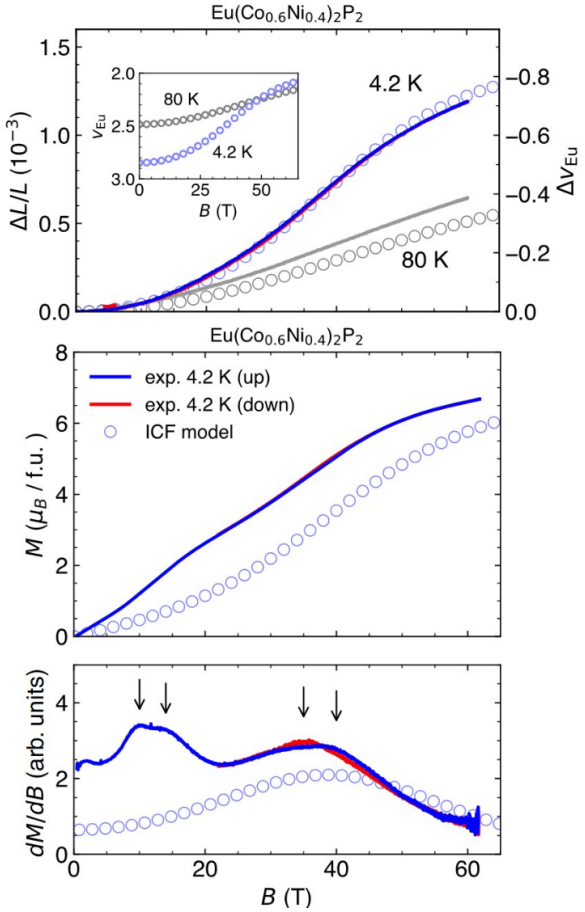


Fig. 1. Magnetic field dependence of the magnetostriction and magnetization of $Eu_{0.4}(Co_{0.6}Ni_{0.4})_2P_2$

slower pulse durations may induce such large state changes in the present material, which is triggered by the Eu valence change under high magnetic fields. Searching for such phase transition in higher magnetic fields using the destructive magnetic field generation method in ISSP should be an interesting future work.

**Reference**

[1] R. Nakamura, A. Ishita, J. Nakamura, H. Ohta, Y. Haraguchi, H. Aruga Katori, H. Ishikawa, A. Matsuo, K. Kindo, M. Nohara, and A. Ikeda, Phys. Rev. B **107**, 235110 (2023).

**Authors**

R. Nakamura[a], A. Ishita[a], J. Nakamura[a], H. Ohta[b], Y. Haraguchi[c], H. Aruga Katori[c], H. Ishikawa, A. Matsuo, K. Kindo, M. Nohara[d], and A. Ikeda[a]

[a]University of Electro-Communications
[b]Doshisha University
[c]Tokyo University of Agriculture and Technology
[d]Hiroshima University

PI of Joint-use project: A. Ikeda
Host lab: Kindo Group

# Nonvolatile Magnetothermal Switching Induced by Flux Trapping in Sn-Pb Solder

High-performance and high-density electronic devices require improvement of thermal management, especially thermal switch technology for controlling heat flow. Spintronic multilayer films [1] and superconductors [2] can control their thermal conductivity ($\kappa$) using only a magnetic field ($H$) without the mechanical motion. However, neither spintronic nor superconducting materials achieved nonvolatile magnetothermal switching (MTS). This study shows nonvolatile MTS in commercial Sn-Pb solder and discuss the origin of its nonvolatility.

We used commercially available flux-core-free solder Sn45-Pb55 (mass ratio Sn : Pb = 45:55, φ1.6 mm, TAIYO ELECTRIC IND. CO., LTD.). The chemical composition and surface of Sn45-Pb55 solder was investigated by scanning-electron microscope and energy-dispersive X-ray spectroscopy, revealing that the Sn45-Pb55 solder is a completely phase-separated composite. Thermal conductivity ($\kappa$) was measured using the Physical Property Measurement System (PPMS, Quantum Design) with the four-probe steady state method. Specific heat ($C$) was measured using PPMS by a relaxation mode. Magnetization was measured using a superconducting quantum interference device magnetometer on the Magnetic Property Measurement System (MPMS3, Quantum Design) with a VSM mode. We performed magneto-optical (MO) imaging at Tokunaga laboratory to observe magnetic flux trapping of Sn45-Pb55 solder in superconducting state [3]. The $H$ dependence of the MO images at 2.5 K was observed, and all the images were temperature difference images at 2.5 K (superconducting state) and 8 K (normal state), and then normalized to the 8 K images.

Figure 1(a) displays the $H$ dependence of $\kappa$ at 2.5 K. After zero field cooling (ZFC), $\kappa$ shows a low value of 10 $WK^{-1}m^{-1}$. However, when the magnetic field is increased from 0 Oe to 1700 Oe, $\kappa$ rises to 35 $WK^{-1}m^{-1}$. Notably, $\kappa$ does not return to its initial value when the magnetic field is decreased from 1700 Oe to 0 Oe, and $\kappa$ maintains a high value throughout any magnetic field process. The initial increase in $\kappa$ by the magnetic field is conventionally understood to be due to the transition of Sn and Pb from the superconducting state to the normal state.

To discuss the nonvolatility of MTS in solder, we first examine the temperature dependence of $C$. Figure 1(b) shows the temperature dependence of specific heat in form of $C/T$ at $H = 0$ after ZFC and field cooling (FC) under 1500 Oe. The $C$ values of the ZFC and FC data is estimated as $C$(0 Oe) - $C$(1500 Oe) to eliminate the specific heat of normal states. The ZFC data show a sharp peak due to the superconducting transition of Sn at 3.7 K and Pb at 7.2 K. However, in the FC data, while the sharp peak corresponding to the superconducting transition of Pb is observed, no peak appears near the superconducting transition temperature of Sn.

The upper panel of Fig. 2. shows the $H$ dependence of the magnetic flux density ($B$) at 2.5 K. $B$ is the sum of $H$ and the magnetization $4\pi M$: $B = H + 4\pi M$. Below $H = 300$ Oe, $B = 0$ G because both Sn and Pb are in the Meissner state.

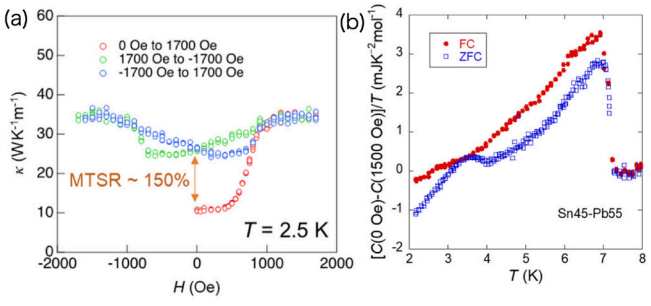


Fig. 1. (a) Magnetic field dependence of $\kappa$ at 2.5 K. (b) Temperature dependence of residual specific heat estimated by $C$(0 Oe)-$C$(1500 Oe) in the form of $C/T$. Both ZFC and FC data are taken at $H = 0$ Oe ZFC and after FC under 1500 Oe, respectively.

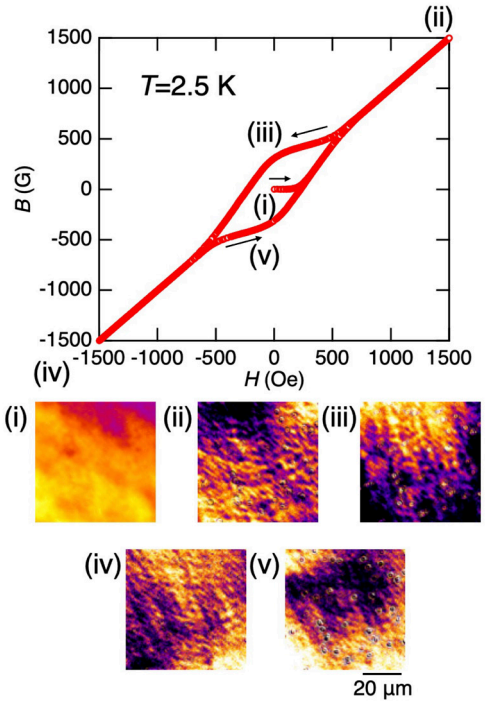


Fig. 2. The upper panel is the *B*-*H* curve at 2.5 K. The lower panels are MO images at 2.5 K. An image (i) is taken after ZFC. Images (ii) and (iv) are taken at $H = 1500$ Oe and $H = -1500$ Oe, respectively. Images (iii) and (v) are taken at $H = 0$ Oe after positive or negative magnetic field, respectively.

When $H$ exceeds 300 Oe which is the critical field of Sn, magnetic flux penetrates and $B$ shows a finite value. In the vicinity of the critical field of Pb at 700 Oe, the magnetic flux penetrates the entire Sn-Pb solder, and $B = H$. After $H$ return to 0 Oe, a magnetic flux of about $B = 400$ G is trapped. The specific heat results show that the superconducting state of Sn is suppressed by FC condition. This suggests that the superconducting bulkiness of Sn is suppressed due to trapping the magnetic flux in Sn region. The lower panels of Fig. 2 show a MO images of Sn-Pb solder. Bright areas indicate positive magnetic flux, and dark areas indicate negative magnetic flux. In the initial state (i), the MO image is uniform as there is no magnetic flux in the solder. In states (ii) and (iv), the magnetic flux penetrates the entire solder. In images (iii) and (iv) at $H = 0$, after experiencing the magnetic field, bright or dark regions in certain clusters indicate that magnetic flux is trapped in specific region.

The findings of this study are summarized with the schematic images in Fig. 3. After ZFC, both Sn and Pb are in the superconducting state, resulting in low κ (Fig. 3(a)). When a magnetic field above the critical field of Sn and Pb is applied, both Sn and Pb transition to the normal state, causing $\kappa$ to increase. Then, at $H = 0$, Pb returns to the superconducting state while Sn traps the magnetic flux, suppressing its superconductivity. Consequently, since the thermal conductivity in the Sn region remains high, the solder shows nonvolatile MTS. In this study, we focused on Sn-Pb solder as a phase-separated superconductor. Interestingly, the solder exhibited the nonvoblatile MTS, and we clarified that the flux trapping played a crucial role in this nonvolatility.

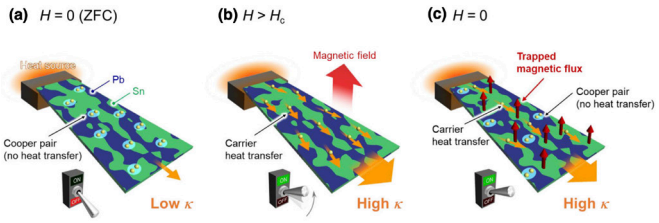


Fig. 3. Schematic images of nonvolatile magnetothermal switching in Sn-Pb solder. (a) The initial state of thermal conductivity ($\kappa$) after ZFC. (b) A state in which a magnetic field exceeding the critical field ($H_c$) of Sn and Pb is applied. (c) State of Sn-Pb solder in $H = 0$ Oe after experiencing $H_c$.

**References**
[1] H.Nakayama *et al*., Appl. Phys. Lett. **118**, 042409 (2021).
[2] M. Yoshida *et al*., J. Appl. Phys. **134**, 065102 (2023).
[3] Y. Kinoshita *et al*., Rev. Sci. Instrum. **93**, 073702 (2022).

**Authors**
H.Arima[a], Md. R. Kasem[a] , H. Sepehri-Amin[b], F. Ando[b], K. Uchida[b], Y. Kinoshita, M. Tokunaga, and Y. Mizuguchi[a]
[a]Tokyo Metropolitan University
[b]NIMS

PI of Joint-use project: Y. Mizuguchi
Host lab: Tokunaga Group

## Magnetic Superstructure Phase Induced by Ultrahigh Magnetic Fields

Magnetic superstructures, where the magnetic unit cell is an integer multiple of the original crystallographic unit cell, have received considerable attention. For frustrated spin systems, a variety of quantum-entangled magnetic superstructures can appear in an external magnetic field. Of particular interest are a series of magnon crystals in the spin-1/2 kagome Heisenberg antiferromagnet [1] and successive transformations of singlet-triplet superstructures in the spin-1/2 orthogonal-dimer Heisenberg antiferromagnet [2]. Furthermore, the interplay between spin and lattice degrees of freedom can induce spin–lattice-coupled magnetic superstructures, as theoretically proposed for the Heisenberg antiferromagnet on the breathing pyrochlore lattice, where neighboring tetrahedra differ in size in an alternating pattern [3]. In this study, we verify this theoretical prediction in a model compound of the breathing pyrochlore antiferromagnet, $LiGaCr_4O_8$, by means of state-of-the-art magnetization and magnetostriction measurements under ultrahigh magnetic fields up to 600 T [4].

Figure 1(a) summarizes the magnetization data of $LiGaCr_4O_8$ measured at ~ 5 K. In the single-turn coil (STC) system, we observe a linear increase in the magnetization $M$ with respect to the external magnetic field $B$ up to a maximum field of 145 T, suggesting that spins are smoothly canting from the 2-up-2-down collinear ground state. Upon

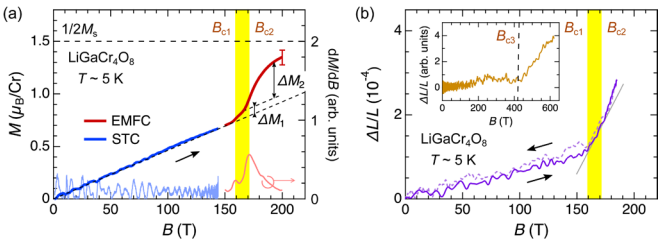


Fig. 1: (a) Magnetization curve of $LiGaCr_4O_8$ at $T \sim 5$ K. Field derivative of the magnetization, d$M$/d$B$, is displayed in the right axis. (b) Magnetostriction curve of $LiGaCr_4O_8$ at $T \sim 5$ K.

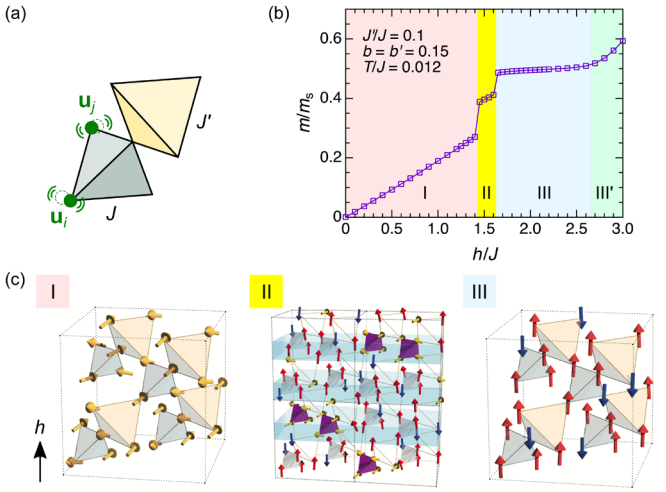


Fig. 2. (a) Site-phonon model taking account of the independent site displacement $\mathbf{u}_i$. (b) Calculated magnetization curve with the exchange parameter $J'/J = 0.1$ and the spin–lattice coupling parameter $b = 0.2$ (see details for Ref. [4]). ] (c) Schematics of the magnetic structures in Phases I ~ III.

the application of a higher magnetic field using the electromagnetic flux compression (EMFC) system, we observe a dramatic magnetization increase between 150 and 200 T, followed by a half plateau at $M \sim 1.5\ \mu_B$/Cr, as reported in conventional chromium spinel oxides [5]. Notably, a double-hump structure can be seen in d$M$/d$B$, indicating a two-step metamagnetic transition at $B_{c1} = 159$ T and $B_{c2} = 171$ T. The existence of an intermediate-field phase is supported by the magnetostriction measurement. Figure 1(b) shows the magnetostriction data measured at ~ 5 K using the STC system. The sample length starts to rapidly increase at $B_{c1}$, then the lattice expansion accelerates above $B_{c2}$. We also measured the magnetostriction up to 600 T using the EMFC system, as shown in the inset of Fig. 1(b). A plateau-like behavior is observed from 200 T up to $B_{c3} \sim 420$ T, followed by an upturn behavior up to the saturation around 550 T. The observation of a wide plateau suggests the strong spin–lattice coupling inherent in $LiGaCr_4O_8$.

To understand these observations, we perform the classical Monte-Carlo simulations for a magnetoelastic Hamiltonian on the breathing pyrochlore lattice, incorporating the Einstein site-phonons [3,4]. Figure 2 shows the calculated magnetization curve obtained for a typical parameter set with relatively large breathing anisotropy and strong spin–lattice coupling. In addition to the low-field phase (Phase I) with an 8-sublattice canted 2-up-2-down state and the 1/2-plateau phase (Phase III) with a 16-sublattice 3-up-1-down state, an intermediate-field phase (Phase II) appears, associated with a two-step metamagnetic transition. The magnetic structure of phase II is characterized by a three-dimensional periodic array of canted 2-up-2-down and 3-up-1-down tetrahedral clusters in a 1:2 ratio, forming a magnetic superstructure with a 6 × 6 × 6 magnetic unit cell.

In summary, we experimentally demonstrate that the breathing pyrochlore antiferromagnet exhibits unconventional field-induced phase transitions, which could signal the emergence of a magnetic superstructure phase. The present work, combining the exotic experimental observations with the microscopic magnetoelastic theory in a complicated three-dimensional frustrated magnet, paves the way for further verifications of intriguing physical phenomena originating from the spin–lattice coupling and/or breathing anisotropy, both of which can be relevant in magnetic materials regardless of the geometry of the underlying crystalline lattice.

**References**
[1] J. Schulenburg *et al*., Phys. Rev. Lett. **88**, 167207 (2002).
[2]. K. Kodama *et al*., Science **298**, 395 (2002).
[3] K. Aoyama *et al*., Phys. Rev. B **104**, 184411 (2021).
[4] M. Gen *et al*., Proc. Natl. Acad. Sci. U.S.A. **120**, e2302756120 (2023).
[5] A. Miyata *et al*., J. Phys. Soc. Jpn. **81**, 114701 (2012)

**Authors**
M. Gen[a] and Y. Kohama
[a]RIKEN Center for Emergent Matter Science

PI of Joint-use project: M. Gen
Host lab: Kohama and Y. H. Matsuda Group